Table 2 Burning-rate results of propellants based on monomodal fine (9μ) AP

Ballistic modifiers (2 parts)	Burning rates (mm/s) at pressure (MPa)						
	1	1.9	2.9	4.9	6.9	8.8	n
Control	8.1	8.5	10.2	12.3	15.5	16	0.34
nBF	12.8	14	15	17.4	20	22	0.28
DFB	12.7	14.5	16.1	18.4	20.9	22.6	0.26
FPGO	12.5	15.8	16.2	18.8	21.4	22.3	0.26

effect of butacene on burning rate of AP composite propellants by Doriath.[17] The nBF being volatile must be effective in gas phase, whereas DFB is expected to occupy an intermediate position because of its higher molecular weight than that of nBF despite being nonbonded like latter.

It is well reported that propellants incorporating fine AP (particle size $\leq 10\mu$) offer greater oxidizer/fuel (O/F) contact line density implying shorter diffusion distance during combustion of propellant. Consequently, reactants can mix completely before appreciable heat is released above the contact lines leading to high combustion rate. The role of vapor–surface O/F reactions also increases in case of propellants incorporating fine oxidizer. The presence of catalyst can further enhance such reactions. In view of this, burning rates of monomodal fine AP (9μ)-based propellant containing two parts of FPGO (over 100 parts of propellant) were also evaluated during this work. Formulation containing FPGO exhibited burning rates of the order of 12.5–22.5 mm/s (Table 2) in the pressure range of 1–8.8 MPa, which are 30–100% higher than those obtained for corresponding bimodal AP-based composition . Again, the burning-rate enhancement effect of FPGO was found to be comparable to that of other ferrocenes derivatives (DFB and nBF). The strand burning rate of FPGO modified (9μ) AP-based propellant obtained during this work were found marginally less than that obtained at 7 MPa on static evaluation of star shaped propellant comprising of (3μ) AP-82% and Al- 4% with binder 14% containing 80:20 combination of HTPB and butacene as reported by Doriath.[17]

Conclusions

This study brings out that the functionalized ferrocenes like ferrocene polyglycol oligomer (FPGO) offer a viable liquid ballistic modifier, which are envisaged to be free from the migration problem of ferrocenes. FPGO offers propellants having burning rates close to those of n-butyl ferrocene- and di ferrocenyl-1-butene based systems. Thermal decomposition patterns of ferrocenes and propellants based on them bring out that physicochemical nature of ferrocenes has bearing on the site of action of catalysts during combustion process. The basic decomposition processes of DFB and FPGO appear to be same.

References

[1]Vuga, S. M., "Effect of Liquid Burn Rate Catalyst on Rheological Properties of High Energy Composite Propellant," *Propellants, Explosives, Pyrotechnics*, Vol. 16, No. 6, Dec. 1991, pp. 293–298.

[2]Ashmore, C. I., Combs, C. S., and Stephenes, W. D., "Solid Propellant Having Incorporated a Ferrocene Combustion Catalyst," U.S. Patent 4,108,696, 22 Aug. 1978.

[3]Raynal, S., and Doriath, G., "New Functional Prepolymers for High Burning Rates Solid Propellants," *AIAA/ASME/SAE/ASEE 22nd Joint Propulsion Conference*, AIAA, New York, 1986, pp. 1–9.

[4]Stephens, W. D., Flanigan, D. A., Hightower, J. O., and Mangum, G. F., "Thermally Stable Burning Rate Accelerators," Thiokoal, C. C., AFRPL-TR-71-3, Quarterly Progress Report, Jan. 1971, prepared for Air Force Systems Command, Air Force Propulsion Laboratory, Edwards Air Force Base, California 93523.

[5]Nilesen, A. T., "Monofunctional Diferrocenyl Compounds," U.S. Patent, 3,878,233, 15 April 1975.

[6]Manke, K., Klaus-Brehler, P., and Bohnlein-Maub., Jutta., "New Chemically Bonded Ferrrocenes for Burn Rate Modification of Composite Rocket and Gas Generating Propellants," *Proccedings of the 26th International Annual conference of ICT*, Karlsruhe, Fraunhofer Inst. Chemisch Technologie, Germany, 4–7 July 1995, pp. 53-1–53-16.

[7]Deway, F. M., "Ferrocene Polyglycols," U.S. Patent, 3,598,850, 10 Aug. 1971.

[8]Stanley, Goldberg, I., Loeble, W. D., and Tidwell, T., "Alumina-Catalysed Dehydration of 1-Ferrocenylethanol. Formation of 1,3-Diferrocenyl-1-Butene," *Journal of Organic Chemistry*, Vol. 32, Sept.–Dec. 1967, pp. 4070, 4071.

[9]Rindrof, H. J., "Accoustic Emission Source Location in Theory and in Practice," *Technical Review to Advanced Techniques in Acoustical, Electrical and Mechanical Measurement*, Bruel and Kjaer, DK-2850, Vol. 2, NAERUM, Denmark, 1981, pp. 3–32.

[10]Coats, A. W., and Redfern, J. P., *Nature*, Vol. 201, No. 4914, 1964, pp. 68, 69.

[11]"Standard Test Method for Arrhenius Kinetic Constants for Thermally Unstable Materials," American Society for Testing and Materials, E 698-79(14.02), Philadelphia, reapproved 1984, pp. 520–525.

[12]Kishore, K., and Prasad, G., "Review on Decomposition/Deflagration of Oxidizer and Binder in Composite Propellants," *Defence Science Journal*, Vol. 29, No. 1, Jan. 1979, pp. 39–54.

[13]Wang, S. Y., Wang, S. S., Liu, F., and Chiu, H. S., "An Investigation of Catalysis in the Combustion of Iron Catalysed Composite Propellants," *Proceedings of the 19th International Annual Conference of ICT*, Karlsruhe, Fraunhofer, Inst. Chemisch Technologie, Germany, 29 June–1 July 1988, pp. 8-1–8-14.

[14]Pittman, C. U., Jr., "Location of Action of Burning-Rate Catalysts in Composite Propellant Combustion," *AIAA Journal*, Vol. 7, No. 2, 1969, pp. 328–334.

[15]Flanagan, D. A., Tech Rept. AFRL-TR-67-18, 1967, prepared for Air Force Systems Command, Air Force Propulsion Laboratory, Edwards Air Force Base, CA 93523.

[16]Pearson, G. S., "The Role of Catalysts in Ignition and Combustion of Solid Propellants," *Combustion, Science, and Technology*, Vol. 3, 1971, pp. 155–163.

[17]Doriath, G., "Energetic Insensitive Propellants for Solid and Ducted Rockets," *Journal of Propulsion and Power*, Vol. 1, No. 4, 1995, pp. 870–882.

Dual-Mode Operations in a Scramjet Combustor

Takeshi Kanda,* Nobuo Chinzei,† Kenji Kudo,‡ and Atsuo Murakami‡

Japan Aerospace Exploration Agency, Miyagi 981-1525, Japan

Introduction

THE application of airbreathing engines, for example, a scramjet, for use with aerospace planes, has been studied. The general operating region of the scramjet is a flight Mach number of around 6–12. The dual-mode combustion system consisting of the scramjet mode and the ramjet mode has been studied, in which the scramjet engine operates even in a lower Mach number regime.[1–3] In the ramjet mode, supersonic air is decelerated and becomes subsonic in an isolator between the inlet and the combustor. Fuel is injected into

Presented as Paper 2001-1816 at the AIAA/NAL-NASDA-ISAS 10th International Space Planes and Hypersonic Systems and Technologies Conference, Kyoto, Japan, 24 April 2001; received 9 July 2003; revision received 2 December 2003; accepted for publication 6 December 2003.

*Leader, Engine System Team, Space Propulsion Research Center, 1 Koganesawa, Kimigaya, Kakuda; kanda.takeshi@jaxa.jp. Senior Member AIAA.

†Director, Space Propulsion Research Center, 1 Koganesawa, Kimigaya, Kakuda; chinzei.nobuo@jaxa.jp. Member AIAA.

‡Senior Researcher, Engine System Team, Space Propulsion Research Center, 1 Koganesawa, Kimigaya, Kakuda.

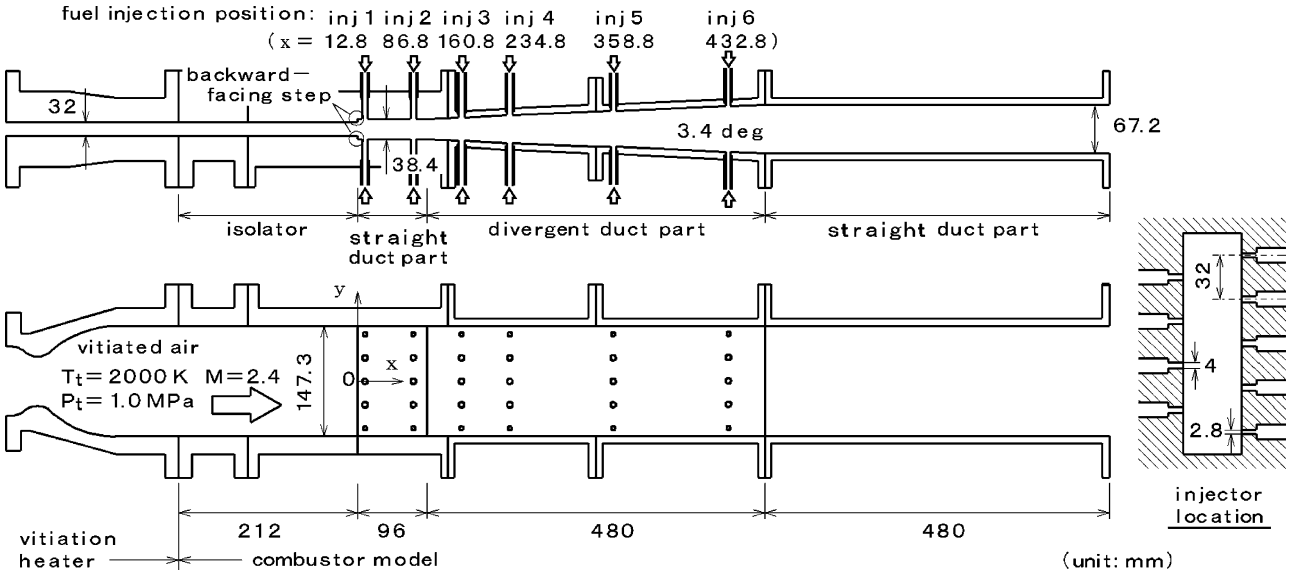

Fig. 1 Schematic diagram of experimental apparatus; hydrogen fuel was injected vertically to the sidewall.

the subsonic air in the combustor, and the combustion gas chokes by the release of heat at the exit of the throat section of the combustor. The supersonic combustion gas expands in the divergent section.

In the present experiments, another ramjet mode was observed, where fuel was injected in the divergent section of the scramjet combustor model. Herein, the experimental results on this mode are presented, and features of the mode are discussed.

Experimental Apparatus

Figure 1 shows the experimental setup.[4] A scramjet combustor model was directly connected to a wind tunnel. High enthalpy airflow was created with a hydrogen vitiation air heater. The total pressure and the total temperature of the air in the reservoir were 1.05 ± 0.05 MPa and 2000 ± 50 K, respectively. The mole fractions of the unreacted oxygen and water in the air were $21 \pm 1\%$ and $26 \pm 1\%$, respectively. To simplify the discussion, high total temperature was used for self-ignition of the hydrogen fuel. The air was accelerated to Mach 2.4 through a supersonic nozzle.

There was an isolator section upstream of the combustor. At the end of the isolator, there were 3.2-mm backward-facing steps on both sides. The height of the boundary layer of 99% of the primary flow velocity was 10 mm at the step.[4] The origin of the x coordinate was at the backward-facing step. A divergent section and another straight duct section followed. The model was made of stainless steel and was uncooled.

The fuel equivalence ratio ϕ was 1 ± 0.05 or 0.5 ± 0.05 in this testing. There were six fuel injection positions in the direction of the airflow, which are indicated with injector 1–injector 6 in Fig. 1. Tests with the staged fuel injection were also conducted, in which the total fuel flow rate was $\phi = 1$ and fuel with $\phi = 0.5$ was injected from each position. At each position, there were five fuel injection holes on one sidewall and four on the other. Total temperature of the fuel was about 290 K, and the fuel was injected at sonic speed vertical to the wall.

Pressure taps were installed on the line at $y = 0$ mm. The pressure was measured with scanning-type sensors (Scanni Valve®), and normalized by the wall pressure at the entrance of the isolator under the no-fuel condition P_{wi}. The normalized ambient pressure of 1 atm was 1.5. The measurement error of the normalized wall pressure, P_w/P_{wi}, was ± 0.02.

Results and Discussion

Wall Pressure Distributions

Figure 2 shows typical wall pressure distributions at $\phi = 1$. The injector positions are indicated in Fig. 2. The distribution in the

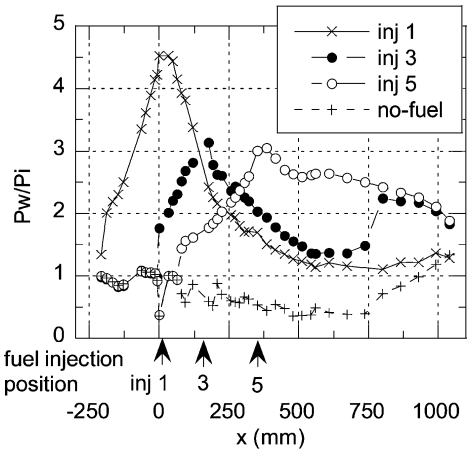

Fig. 2 Wall pressure distributions with fuel injection from injector 1, injector 3, and injector 5 ($\phi = 1$).

no-fuel condition is also plotted. When the fuel was injected from injector 1, the pressure increased gradually in the isolator, showed a peak around the injector, and decreased toward the exit of the straight section of the combustor, further decreasing in the divergent section. These features indicated that the combustion condition would be in the ordinary ramjet mode. The distributions of the pressure with the fuel injection from injector 3 or 5 were quite different from that with fuel injection from injector 1. When the fuel was injected downstream, as in the case of injector 5, the pressure began to increase in the divergent section, showed a peak around the injector, then decreased gradually toward the exit. The downstream high pressure did not affect the airflow condition in the isolator. The normalized exit pressure, P_{we}/P_{wi}, was 1.9, which was higher than the ambient pressure. The distribution of the pressure with the fuel injection from injector 3 showed two peaks. The increase of the wall pressure around the exit was similar to that with injector 5.

Figure 3 shows the wall pressure distributions with injectors 1 and 6 at $\phi = 0.5$. When the fuel was injected from injector 1, the pressure quickly increased just upstream of the step and then decreased. The profile of the wall pressure increase was different from that with $\phi = 1$. When the fuel was injected from injector 6, the wall pressure began to increase around the injector, as well as that with $\phi = 1$ from injector 5. P_{we}/P_{wi} was about 1.6, being lower than that at $\phi = 1$, but higher than the ambient pressure.

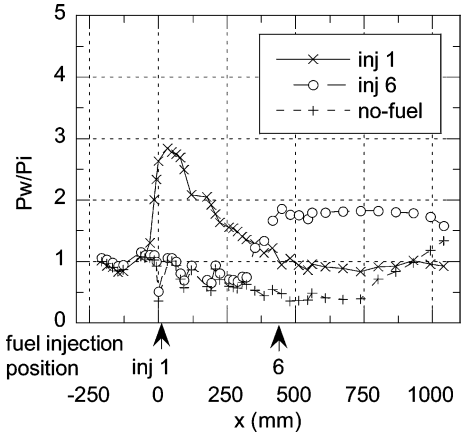

Fig. 3 Wall pressure distributions with fuel injection from injector 1 and injector 6 (ϕ = 0.5).

Ramjet Mode Operation

When the fuel was injected from downstream injector, the combustion gas was probably subsonic and choked at the exit. The exit pressure is estimated with assumption of choking at the exit. The mass flow rate $\dot{m}$ is expressed as follows:

$$\dot{m} = \rho u A$$

$$= P\sqrt{(\gamma \cdot W)/(R0 \cdot T_t)} \cdot A \cdot M\sqrt{1 + [(\gamma - 1)/2]M^2} \qquad (1)$$

Here, ρ, u, and A are density, velocity, and the cross section, respectively. P, γ, W, $R0$, T_t, and M are pressure, the ratio of the specific heats, molecular weight, the universal gas constant, total temperature, and a Mach number, respectively. When $M = 1$,

$$P = (\dot{m}/A)\sqrt{(R0 \cdot T_t)/(\gamma \cdot W)} \cdot \sqrt{2/(\gamma + 1)} \qquad (2)$$

In the present test condition, $T_t = 2790$ K, $\gamma = 1.20$, $W = 21.1$, and $\dot{m} = 1.44$ kg $\cdot$ s^{-1} at $\phi = 1$ and the combustion efficiency η_c of unity under the equilibrium condition. When A is the geometrical cross section at the exit of the model, the normalized pressure at the exit, P_e/P_{wi}, with Eq. (2) becomes 1.96. When $\phi = 0.5$, P_e/P_{wi} becomes 1.76 at $\eta_c = 1$. The measured pressures at the exit and the calculated ones under the choking condition showed reasonable agreement. The combustion gas was choked at the exit of the combustor with no geometrical throat. A similar choking condition with no wall throat was observed in the experiments of the airbreathing rocket.[5]

The supersonic gas became subsonic, and then was accelerated to the sonic speed by heat release. This is a kind of the ramjet mode, differing from the ordinary ramjet mode. In this downstream-combustion ramjet mode, a long isolator will not be necessary because deceleration of the airflow was in the divergent section. The maximum pressure was lower than that of the ordinary ramjet mode, and the lower pressure level will reduce the weight of the engine and heat flux.

This discussion on choking condition can be applied to the ordinary ramjet mode. When the choking point is at the exit of the upstream straight section and A is the geometrical cross section, P/P_{wi} at choking with Eq. (2) becomes 3.44 at $\phi = 1$ and 3.32 at $\phi = 0.8$. The calculated pressure is close to the measured one with injector 1 in Fig. 2. The pressure at choking becomes 3.07 at $\phi = 0.5$. However, the measured pressure in Fig. 3 was lower than the calculated one. The operating condition with the fuel injection from injector 1 at $\phi = 0.5$ was the scramjet mode. The ordinary ramjet mode was attained with injection of fuel at $\phi = 1$ into the upstream straight duct section, that is, injector 1, injector 2, the staged injection from injector 1 and injector 2.

Thrust of the Ramjet Mode

The impulse function F is expressed as follows:

$$F = \dot{m}u + P \cdot A = \dot{m}\sqrt{\gamma(R0/W) \cdot T_t}$$

$$\times \left\{1\Big/\sqrt{1 + [(\gamma - 1)/2]M^2}\right\}[M + 1/(\gamma M)] \qquad (3)$$

When $M = 1$,

$$F = \dot{m}\sqrt{[2\gamma/(\gamma + 1)][(R0 \cdot T_t)/W]}(1 + 1/\gamma) \qquad (4)$$

In the downstream-combustion ramjet mode, at the exit of the model, F becomes 2890 N with Eq. (4) at $\phi = 1$ and $\eta_c = 1$ under the equilibrium condition. When the difference from the inflow impulse function F_i is subtracted and normalized with F_i, it becomes 0.16. Here, F_i is 2490 N with Eq. (3), in which $M = 2.4$, $T_t = 2000$ K, $\gamma = 1.30$, and $W = 26.4$, respectively. The force increase by wall pressure integration was 0.28 with fuel injection from injector 5 in the normalized form. The base pressure and the pressure in the divergent section were used in the integration. The total friction force was estimated to be 0.12 in the model. The impulse function at $\phi = 0.5$ is calculated to be 0.04 in the normalized form at $\eta_c = 1$ with Eq. (4). The force increase by wall pressure integration was 0.15 at $\phi = 0.5$ with fuel injection from injector 6. The total friction force was estimated to be 0.11, being close to the vale at $\phi = 1$.

This discussion can be applied to the ordinary ramjet mode. The impulse function at the exit of the upstream straight section under the choking condition is balanced with sum of the impulse function from the facility nozzle and the reaction force at the steps. When the measured base pressure is used, the sum of the impulse function becomes 0.12 in the normalized form. It agreed with the calculated impulse function at the exit of the upstream straight duct with $\phi = 0.8$, by the use of Eq. (4). The combustion efficiency was presumed to be around 0.8 at the $\phi = 1$ condition. At $\phi = 0.5$, even under the $\eta_c = 1$ condition, the normalized impulse function at choking is 0.04 with Eq. (4). When the choking pressure is used for the base pressure, the sum of the impulse function is 0.08 downstream of the step in the normalized form, being larger than the calculated function at choking. The choking condition was not satisfied at $\phi = 0.5$.

The thrust by the downstream-combustion ramjet mode is specified with the impulse function by Eq. (4). It has a relation to the mass flow rate and the total temperature, but does not have a relation to the cross section. In the ordinary ramjet mode, the impulse function is also specified by Eq. (4) at the choking position. The additional force is created through supersonic combustion and the expansion in the divergent nozzle. The increase of the impulse function of the ordinary ramjet mode is calculated to be 0.29 in the normalized form at the exit of the model under the assumption of the isentropic expansion at $\phi = 0.8$, larger than that of the downstream-combustion ramjet mode at $\phi = 1$.

In the actual engine mounted on the aerospace plane, there will be an external nozzle downstream of the combustor. With the lower Mach number at the exit of the combustor, the pressure after expansion on the nozzle becomes higher. In the downstream-combustion ramjet mode, the Mach number is unity, and the pressure level is high. The thrust of the mode will increase with the external nozzle.

Conclusions

The dual-mode operation of a scramjet combustor was studied experimentally in a Mach 2.4 wind tunnel. The total temperature and the total pressure of the air were 2000 K and 1 MPa, respectively. The downstream-combustion ramjet mode was attained, when fuel was injected in the divergent section. In the mode, air was decelerated in the divergent section with consequent subsonic combustion. The subsonic combustion gas was choked at the exit of the combustor with no wall throat. The downstream high pressure did not affect the airflow condition in the isolator. Thrust was smaller, but the maximum pressure was lower in the downstream-combustion ramjet mode than those in the ordinary ramjet mode.

References

[1]Billig, F. S., "Research on Supersonic Combustion," *Journal of Propulsion and Power*, Vol. 9, No. 4, 1993, pp. 499–514.

[2]Sullins, G. A., "Demonstration of Mode Transition in a Scramjet Combustor," *Journal of Propulsion and Power*, Vol. 9, No. 4, 1993, pp. 515–520.

[3]Heiser, W. H., Pratt, D. T., with Daley, D. H., and Mehta, U. B., "Hypersonic Airbreathing Propulsion," AIAA Education Series, AIAA, Washington, DC, 1994, pp. 334–370.

[4]Chinzei, N., Komuro, T., Kudo, K., Murakami, A., Tani, K., Masuya, G., and Wakamatsu, Y., "Effects of Injector Geometry on Scramjet Combustor Performance," *Journal of Propulsion and Power*, Vol. 9, No. 1, 1993, pp. 146–152.

[5]Chinzei, N., Masuya, G., Kudo, K., Murakami, A., and Komuro, T., "Experiment on Multiple Fuel Supplies to Airbreathing Rocket Combustors," *Journal of Propulsion and Power*, Vol. 3, No. 1, 1987, pp. 26–32.

Electric Sail for Spacecraft Propulsion

Pekka Janhunen*
Finnish Meteorological Institute/Geophysical Research, FIN-00101, Helsinki, Finland

Nomenclature

A	=	cross-sectional area of wire, m
A_s	=	total surface area of all wires, m^2
$A_s^{(1)}$	=	surface area of one wire, m^2
a	=	acceleration, $m \cdot s^{-2}$
E	=	electric field along wire, V/m
e	=	electron charge, $A \cdot s$
F	=	force excerted by solar wind on system, N
I	=	total electron current to the mesh, A
I_1	=	electron current to one wire, A
j	=	electron current density from plasma to wire mesh, $A \cdot m^{-2}$
$j_\parallel$	=	maximum current density in wire, $A \cdot m^{-2}$
L	=	linear dimension of whole structure, m
m	=	mass of wire mesh, m
m_p	=	proton mass, kg
N	=	number of wires
n	=	solar wind plasma number density, cm^{-3}
P	=	power consumption of electron removal, W
$p_{\rm dyn}$	=	solar wind dynamic pressure, nPa
r	=	radius of the mesh wire, m
V	=	mesh potential with respect to plasma, V
v	=	solar wind speed, m/s
v_e	=	thermal speed of solar wind electrons, m/s
$v_{\rm final}$	=	final speed of spacecraft, m/s
ΔV	=	potential drop along wire, V
Δx	=	mesh spacing, m
ρ	=	mass density of wire material, $kg \cdot m^{-3}$
$\rho_{\rm SW}$	=	solar wind mass density, $kg \cdot m^{-3}$
σ	=	wire material conductivity, $\Omega^{-1}\ m^{-1}$

I. Introduction

IT has been previously proposed that a magnetic sail, that is, an artificial magnetosphere, could be used for extracting solar wind momentum for spacecraft propulsion purposes.[1,2] Here we consider an alternative approach, which does not require a magnetic field.

II. Electric Sail

Consider a mesh made of thin conducting wires and placed across solar wind flow (Fig. 1). If the mesh is kept at a positive potential with respect to the solar wind plasma, an outward electric field sets up around each wire whose spatial scale size is comparable to the Debye length of the plasma. Incoming solar wind protons see the mesh as an inpenetrable barrier if the mesh spacing is of the same order as the Debye length or smaller and if the mesh is kept at a potential V, which is such that eV exceeds the kinetic energy of the solar wind protons (about 1 keV). To be sure that the potential is high enough, we assume $V = 6$ kV.

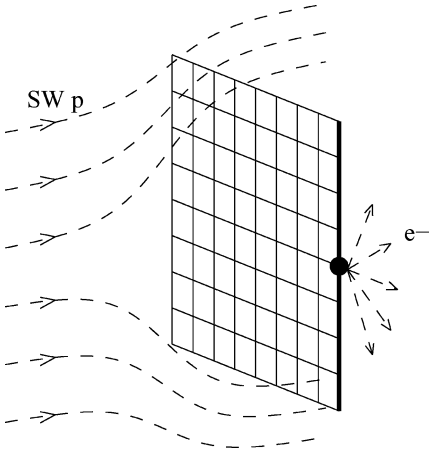

Fig. 1 Schematic of the electric sail.

Let r denote the radius of the mesh wire (where we assume $r = 5 \times 10^{-6}$ m) and $A = \pi r^2$ its cross-sectional area. Assume for simplicity that the mesh is a square with side length L and that the mesh spacing is Δx so that there are $N = L/\Delta x$ wires along each side. We assume $L = 30$ km and $\Delta x = 5$ m. The total length of wire in the structure is $2NL = 2L^2/\Delta x = 360{,}000$ km, and its mass m is

$$m = 2L^2 A\rho/\Delta x = 250 \text{ kg} \tag{1}$$

where ρ is the mass density of the wire metal. (We assume copper density $\rho = 8900\ kg \cdot m^{-3}$.) The (maximum possible) force F acting on the mesh structure is obtained by multiplying the solar wind dynamic pressure $p_{\rm dyn} = \rho_{\rm SW} v^2$ by the mesh area L^2, where $\rho_{\rm SW} = nm_p$ is the solar wind mass density and v its flow velocity (proton velocity). We assume the average values at 1 astronomical unit (AU) $n = 7.3\ cm^{-3}$, $\rho_{\rm SW} =$ and $v = 400$ km/s, where $p_{\rm dyn} = 2$ nPa (Ref. 3). Thus, one obtains $F = \rho_{\rm SW} v^2 L^2 = 1.8$ N. The acceleration a of the structure is

$$a = F/m = (\rho_{\rm SW}/2\rho)(v^2 \Delta x/A) = 7 \times 10^{-3}\ m \cdot s^{-2} \tag{2}$$

A. Pumping Out Electrons

Solar wind electrons bombard the wire mesh, trying to neutralise its positive charge. Therefore, electrons must be continuously "pumped" out of the structure by attaching it to a voltage source whose other end is connected to an electron-emitting device (Fig. 1). The total surface area of the wire mesh is

$$A_s = (2N)2\pi rL = 4\pi rL^2/\Delta x = 11300\ m^2 \tag{3}$$

and the current density due to the thermal flux of solar wind electrons can be roughly estimated as $j = env_e$ where v_e is the solar wind electron thermal speed, we assume $v_e = 10^6$ m/s. We obtain $j = 1.2\ \mu A\ m^{-2}$. The total current I to the whole mesh is

$$I = env_e A_s = 13 \text{ mA} \tag{4}$$

In the voltage source, the current I goes through potential drop V, consuming power $P = VI = 80$ W. A useful measure of the power requirement is the power per mass ratio,

$$\frac{P}{m} = \frac{2Venv_e}{r\rho} = 0.3\ W\ kg^{-1} \tag{5}$$

Thus the power consumption is quite reasonable. Present-day solar-powered electric engines, SMART-1 [Ref. 4] for example, reach a

Received 25 February 2004; revision received 11 March 2004; accepted for publication 12 March 2004.

*Academy Researcher, P.O. Box 503.